Tracking Everything Everywhere All at Once

Qianqian Wang[1,2]   Yen-Yu Chang[1]   Ruojin Cai[1]   Zhengqi Li[2]
Bharath Hariharan[1]   Aleksander Holynski[2,3]   Noah Snavely[1,2]

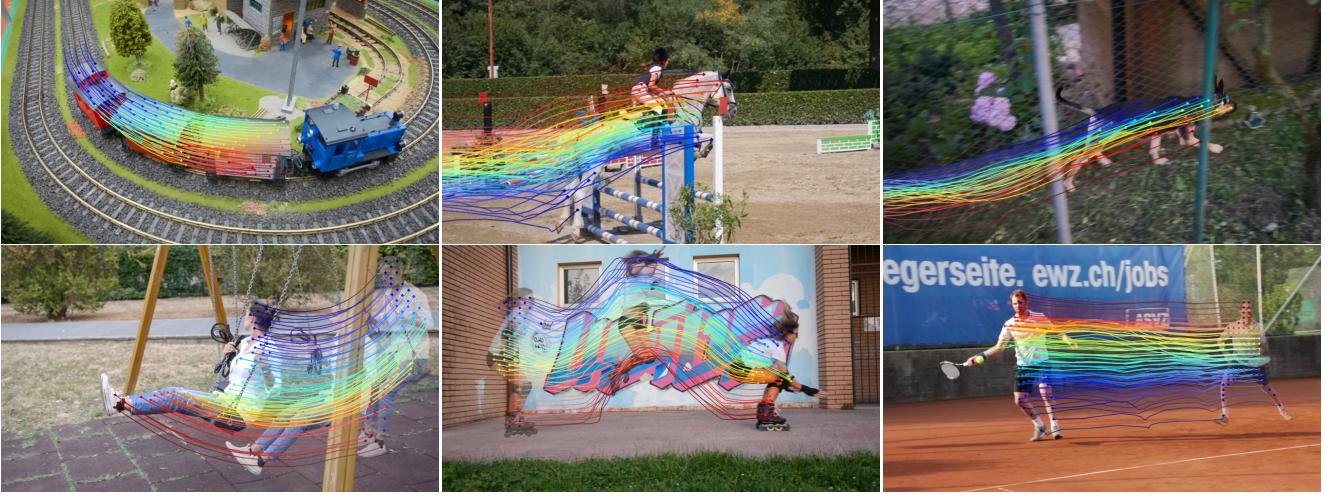[1]Cornell University   [2]Google Research   [3]UC Berkeley

Figure 1: We present a new method for estimating full-length motion trajectories for every pixel in every frame of a video, as illustrated by the motion paths shown above. For clarity, we only show sparse trajectories for foreground objects, though our method computes motion for *all* pixels. Our method yields accurate, coherent long-range motion even for fast-moving objects, and robustly tracks through occlusions as shown in the *dog* and *swing* examples. For context, in the second row we depict the moving object at different moments in time.

Abstract

We present a new test-time optimization method for estimating dense and long-range motion from a video sequence. Prior optical flow or particle video tracking algorithms typically operate within limited temporal windows, struggling to track through occlusions and maintain global consistency of estimated motion trajectories. We propose a complete and globally consistent motion representation, dubbed OmniMotion, that allows for accurate, full-length motion estimation of every pixel in a video. OmniMotion represents a video using a quasi-3D canonical volume and performs pixel-wise tracking via bijections between local and canonical space. This representation allows us to ensure global consistency, track through occlusions, and model any combination of camera and object motion. Extensive evaluations on the TAP-Vid benchmark and real-world footage show that our approach outperforms prior state-of-the-art methods by a large margin both quantitatively and qualitatively. See our project page for more results: omnimotion.github.io.

1. Introduction

Motion estimation methods have traditionally followed one of two dominant approaches: sparse feature tracking and dense optical flow [51]. While each type of method has proven effective for their respective applications, neither representation fully models the motion of a video: pairwise optical flow fails to capture motion trajectories over long temporal windows, and sparse tracking does not model the motion of all pixels.

A number of approaches have sought to close this gap, i.e., to estimate both *dense* and *long-range* pixel trajectories in a video. These range from methods that simply chain together two-frame optical flow fields, to more recent approaches that directly predict per-pixel trajectories across multiple frames [21]. Still, these methods all use limited context when estimating motion, disregarding information that is either temporally or spatially distant. This locality can result in accumulated errors over long trajectories and spatio-temporal inconsistencies in the motion estimates. Even when prior methods do consider long-range context [51], they op-

1

erate in the 2D domain, resulting in a loss of tracking during occlusion events. All in all, producing both *dense* and *long-range* trajectories remains an open problem in the field, with three key challenges: (1) maintaining accurate tracks across long sequences, (2) tracking points through occlusions, and (3) maintaining coherence in space and time.

In this work, we propose a holistic approach to video motion estimation that uses *all* the information in a video to jointly estimate full-length motion trajectories for every pixel. Our method, which we dub *OmniMotion*, uses a quasi-3D representation in which a canonical 3D volume is mapped to per-frame local volumes through a set of local-canonical bijections. These bijections serve as a flexible relaxation of dynamic multi-view geometry, modeling a combination of camera and scene motion. Our representation guarantees cycle consistency, and can track all pixels, even while occluded (*"Everything, Everywhere"*). We optimize our representation per video to jointly solve for the motion of the entire video *"All at Once"*. Once optimized, our representation can be queried at any continuous coordinate in the video to receive a motion trajectory spanning the entire video.

In summary, we propose an approach that: 1) produces globally consistent full-length motion trajectories for all points in an entire video, 2) can track points through occlusions, and 3) can tackle in-the-wild videos with any combination of camera and scene motion. We demonstrate these strengths quantitatively on the TAP video tracking benchmark [14], where we achieve state-of-the-art performance, outperforming all prior methods by a large margin.

2. Related Work

Sparse feature tracking.   Tracking features [4, 39] across images is essential for a wide range of applications such as Structure from Motion (SfM) [1, 52, 55] and SLAM [15]. While sparse feature tracking [12, 40, 53, 63] can establish long-range correspondence, this correspondence is limited to a set of distinctive interest points, and often restricted to rigid scenes. Hence, below we focus on work that can produce dense pixel motion for general videos.

Optical flow.   Optical flow has traditionally been formulated as an optimization problem [6, 7, 22, 71]. However, recent advances in deep learning have enabled direct prediction of optical flow using neural networks with improved quality and efficiency [18, 23, 24, 57]. One leading method, RAFT [62], estimates flow through iterative updates of a flow field based on 4D correlation volumes. While optical flow methods allow for precise motion estimation between consecutive frames, they are not suited to long-range motion estimation: chaining pairwise optical flow to produce longer trajectories results in drift and fails to handle occlusions; and directly computing optical flow between distant frames (i.e., larger displacements) often results in temporal

inconsistency [8, 71].

Multi-frame flow.   To move beyond the limitations of two-frame optical flow, a number of methods have explored multi-frame flow estimation [25, 27, 48, 66]. A notable recent approach, PIPs [21], can estimate multi-frame trajectories through occlusions by leveraging context within a wider temporal window (8 frames). However, to produce motion for a video longer than this temporal window, PIPs still must chain correspondences, a process that (1) is prone to drift and (2) will lose track of points that remain occluded beyond the window. In contrast, our method optimizes motion globally across the entire video, enabling accurate long-range tracking, even through long periods of occlusion.

Feature matching.   While optical flow methods are typically intended to operate on consecutive frames, other techniques can estimate dense correspondences between distant pairs of video frames [38]. Several methods learn such correspondences in a self- or weakly-supervised manner [5, 9, 12, 34, 49, 67, 69, 73] using cues like cycle consistency [26, 70, 76], while others [16, 28, 58, 64, 65] use stronger supervision signals such as geometric correspondences generated from 3D reconstruction pipelines [36, 52]. However, pairwise matching approaches typically do not incorporate temporal context, which can lead to inconsistent tracking over long videos and poor occlusion handling. In contrast, our method not only enables smooth trajectories, but also produces plausible locations for occluded pixels.

Video-based motion optimization.   Most conceptually related to our approach are classical methods that optimize motion globally over an entire video [2, 11, 33, 50, 51, 56, 59, 68]. Particle video [51], for instance, can produce a set of semi-dense long-range trajectories (called *particles*) from initial optical flow fields. However, this method does not allow tracking through occlusions; the same visual entity will be treated as a different particle when it re-appears after occlusions. Rubinstein et al. [50] further proposed a combinational assignment approach that can track through occlusion and generate longer trajectories. However, these methods only produce semi-dense tracks for videos with simple motion, whereas our method estimates long-range motion for all pixels in in-the-wild videos. Also related is ParticleSfM [75], which also optimizes long-range correspondences from pairwise optical flows. Unlike our approach, ParticleSfM focuses on camera pose estimation within an SfM framework, where only correspondences from static regions are optimized, and dynamic objects are treated as outliers.

Neural video representations.   While our method shares similarities with recent methods that model videos using coordinate-based multi-layer perceptrons (MLPs) [41, 54, 61], prior work has primarily focused on problems such as novel view synthesis [35, 37, 43, 44, 72] and video decomposition [29, 74]. In contrast, our work targets the challenge of

dense, long-range motion estimation. Though some methods for dynamic novel view synthesis produce 2D motion as a by-product, these systems require known camera poses and the resulting motion is often erroneous [19]. Alternatively, video decomposition-based representations such as Layered Neural Atlases [29] and Deformable Sprites [74] solve for a mapping between each frame and a global texture atlas. Frame-to-frame correspondence can be derived by inverting this mapping, but this process is expensive and unreliable. Furthermore, these methods are limited to representing videos using a limited number of layers with fixed ordering, restricting their ability to model complex, real-world videos.

3. Overview

We propose a test-time optimization approach for estimating dense and long-range motion from a video sequence. Our method takes as input a collection of frames and pairwise noisy motion estimates (e.g., optical flow fields), and uses these to solve for a complete, globally consistent motion representation for the entire video. Once optimized, our representation can be queried with any pixel in any frame to produce a smooth, accurate motion trajectory across the full video. Our method identifies when points are occluded, and even tracks points through occlusions. In the following sections, we describe our underlying representation, dubbed *OmniMotion* (Sec. 4), then describe our optimization process (Sec. 5) for recovering this representation from a video.

4. OmniMotion representation

As discussed in Sec. 1, classical representations of motion, such as pairwise optical flow, lose track of objects when they are occluded, and can produce inconsistencies when correspondences are composed over multiple frames. To provide accurate, consistent tracks even through occlusion, we therefore need a *global* motion representation, i.e., a data structure that encodes the trajectories of all points in a scene. One such global representation is the decomposition of a scene into a set of discrete, depth-separated "layers" [29, 74]. Unfortunately, most real-world dynamic scenes cannot be represented as a set of fixed, ordered layers: e.g., consider the simple case of an object rotating in 3D. At the other extreme is full 3D reconstruction that disentangles 3D scene geometry, camera pose and scene motion. This, however, is an extremely ill-posed problem. Thus, we ask: can we accurately track real-world motion without explicit dynamic 3D reconstruction?

We answer this question using our proposed representation, *OmniMotion* (illustrated in Fig. 2). OmniMotion represents the scene in a video as a canonical 3D volume that is mapped to local volumes for each frame through local-canonical bijections. The local-canonical bijections are parametrized as neural networks and capture both camera and scene motion without disentangling the two. As such, the video can be considered as a rendering of the resulting local volumes from a fixed, static camera.

Because OmniMotion does not explicitly disentangle camera and scene motion, the resulting representation is not a physically accurate 3D scene reconstruction. Instead we call it a *quasi*-3D representation. This relaxation of dynamic multi-view geometry allows us to sidestep ambiguities that make dynamic 3D reconstruction challenging. Yet we retain properties needed for consistent and accurate long-term tracking through occlusion: first, by establishing bijections between each local frame and a canonical frame, OmniMotion guarantees globally cycle-consistent 3D mappings across all local frames, which emulates the one-to-one correspondences between real-world, metric 3D reference frames. Second, OmniMotion retains information about all scene points that are projected onto each pixel, along with their relative depth ordering, enabling points to be tracked even when they are temporarily occluded from view.

In the following sections, we describe our quasi-3D canonical volume and 3D bijections, and then describe how they can be used to compute motion between any two frames.

4.1. Canonical 3D volume

We represent a video's content using a canonical volume G that acts as a three-dimensional atlas of the observed scene. As in NeRF [41], we define a coordinate-based network F_{θ} over G that maps each canonical 3D coordinate $\boldsymbol{u} \in G$ to a density σ and color $\boldsymbol{c}$. The density stored in G is key, as it tells us where the surfaces are in canonical space. Together with the 3D bijections, this allows us to track surfaces over multiple frames as well as reason about occlusion relationships. The color stored in G allows us to compute a photometric loss during optimization.

4.2. 3D bijections

We define a continuous bijective mapping $\mathcal{T}_{\boldsymbol{i}}$ that maps 3D points $\boldsymbol{x}_i$ from each local coordinate frame L_i to the canonical 3D coordinate frame as $\boldsymbol{u} = \mathcal{T}_{\boldsymbol{i}}(\boldsymbol{x}_i)$, where i is the frame index. Note that the canonical coordinate $\boldsymbol{u}$ is time-independent and can be viewed as a globally consistent "index" for a particular scene point or 3D trajectory across time. By composing these bijective mappings and their inverses, we can map a 3D point from one local 3D coordinate frame (L_i) to another (L_j):

$$\boldsymbol{x}_j = \mathcal{T}_{\boldsymbol{j}}^{-1} \circ \mathcal{T}_{\boldsymbol{i}}(\boldsymbol{x}_i). \tag{1}$$

Bijective mappings ensure that the resulting correspondences between 3D points in individual frames are all cycle consistent, as they arise from the same canonical point.

To allow for expressive maps that can capture real-world motion, we parameterize these bijections as invertible neural
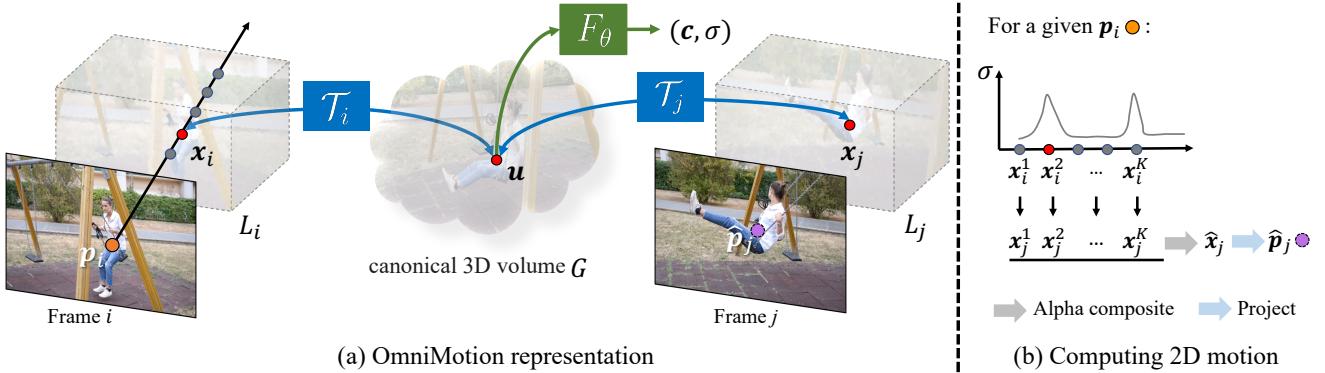
For a given $\boldsymbol{p}_i$ ⬤ :

(a) OmniMotion representation

(b) Computing 2D motion

Figure 2: *Method overview*. (a) Our OmniMotion representation is comprised of a canonical 3D volume G and a set of bijections $\mathcal{T}_i$ that map between each frame's local volume L_i and the canonical volume G. Any local 3D location $\boldsymbol{x}_i$ in frame i can be mapped to its corresponding canonical location $\boldsymbol{u}$ through $\mathcal{T}_i$, and then mapped back to another frame j as $\boldsymbol{x}_j$ through the inverse mapping $\mathcal{T}_j^{-1}$. Each location $\boldsymbol{u}$ in G is associated with a color $\boldsymbol{c}$ and density σ, computed using a coordinate-based MLP $F_{\boldsymbol{\theta}}$. (b) To compute the corresponding 2D location for a given query point $\boldsymbol{p}_i$ mapped from frame i to j, we shoot a ray into L_i and sample a set of points $\{\boldsymbol{x}_i^k\}_{k=1}^K$, which are then mapped first to the canonical space to obtain their densities, and then to frame j to compute their corresponding local 3D locations $\{\boldsymbol{x}_j^k\}_{k=1}^K$. These points $\{\boldsymbol{x}_j^k\}_{k=1}^K$ are then alpha-composited and projected to obtain the 2D corresponding location $\hat{\boldsymbol{p}}_j$.

networks (INNs). Inspired by recent work on homeomorphic shape modeling [32, 45], we use Real-NVP [13] due to its simple formulation and analytic invertibility. Real-NVP builds bijective mappings by composing simple bijective transformations called affine coupling layers. An affine coupling layer splits the input into two parts; the first part is left unchanged, but is used to parametrize an affine transformation that is applied to the second part.

We modify this architecture to also condition on a per-frame latent code $\boldsymbol{\psi}_i$ [32, 45]. Then all invertible mappings $\mathcal{T}_i$ are parameterized by the same invertible network $M_{\boldsymbol{\theta}}$, but with different latent codes: $\mathcal{T}_i(\cdot) = M_{\boldsymbol{\theta}}(\cdot; \boldsymbol{\psi}_i)$.

4.3. Computing frame-to-frame motion

Given this representation, we now describe how we can compute 2D motion for any query pixel $\boldsymbol{p}_i$ in frame i. Intuitively, we "lift" the query pixel to 3D by sampling points on a ray, "map" these 3D points to a target frame j using bijections $\mathcal{T}_i$ and $\mathcal{T}_j$, "render" these mapped 3D points from the different samples through alpha compositing, and finally "project" back to 2D to obtain a putative correspondence.

Specifically, since we assume that camera motion is subsumed by the local-canonical bijections $\mathcal{T}_i$, we simply use a fixed, orthographic camera. The ray at $\boldsymbol{p}_i$ can then be defined as $\boldsymbol{r}_i(z) = \boldsymbol{o}_i + z\boldsymbol{d}$, where $\boldsymbol{o}_i = [\boldsymbol{p}_i, 0]$ and $\boldsymbol{d} = [0, 0, 1]$. We sample K samples on the ray $\{\boldsymbol{x}_i^k\}$, which are equivalent to appending a set of depth values $\{z_i^k\}_{k=1}^K$ to $\boldsymbol{p}_i$. Despite not being a physical camera ray, it captures the notion of multiple surfaces at each pixel and suffices to handle occlusion.

Next we obtain densities and colors for these samples by mapping them to the canonical space and then querying the density network $F_{\boldsymbol{\theta}}$. Taking the k-th sample $\boldsymbol{x}_i^k$ as an

example, its density and color can be written as $(\sigma_k, \boldsymbol{c}_k) = F_{\boldsymbol{\theta}}(M_{\boldsymbol{\theta}}(\boldsymbol{x}_i^k; \boldsymbol{\psi}_i))$. We can also map each sample along the ray to a corresponding 3D location $\boldsymbol{x}_j^k$ in frame j (Eq. 1).

We can now aggregate the correspondences $\boldsymbol{x}_j^k$ from all samples to produce a single correspondence $\hat{\boldsymbol{x}}_j$. This aggregation is similar to how the colors of sample points are aggregated in NeRF: we use alpha compositing, with the alpha value for the k-th sample as $\alpha_k = 1 - \exp(-\sigma_k)$. We then compute $\hat{\boldsymbol{x}}_j$ as:

$$\hat{\boldsymbol{x}}_j = \sum_{k=1}^{K} T_k \alpha_k \boldsymbol{x}_j^k, \text{ where } T_k = \prod_{l=1}^{k-1}(1 - \alpha_l) \quad (2)$$

A similar process is used to composite $\boldsymbol{c}^k$ to get the image-space color $\hat{C}_i$ for $\boldsymbol{p}_i$. $\hat{\boldsymbol{x}}_j$ is then projected using our stationary orthographic camera model to yield the predicted 2D corresponding location $\hat{\boldsymbol{p}}_j$ for the query location $\boldsymbol{p}_i$.

5. Optimization

Our optimization process takes as input a video sequence and a collection of noisy correspondence predictions (from an existing method) as guidance, and generates a complete, globally consistent motion estimate for the entire video.

5.1. Collecting input motion data

For most of our experiments, we use RAFT [62] to compute input pairwise correspondence. We also experimented with another dense correspondence method, TAP-Net [14], and demonstrate in our evaluation that our approach consistently works well given different types of input correspondence. Taking RAFT as an example, we begin by exhaustively computing all pairwise optical flows. Since optical

flow methods can produce significant errors under large displacements, we apply cycle consistency and appearance consistency checks to filter out spurious correspondences. We also optionally augment the flows through chaining, when deemed reliable. Additional details about our flow collection process are provided in the supplemental material. Despite the filtering, the (now incomplete) flow fields remain noisy and inconsistent. We now introduce our optimization method that consolidates these noisy, incomplete pairwise motion into complete and accurate long-range motion.

5.2. Loss functions

Our primary loss function is a flow loss. We minimize the mean absolute error (MAE) between the predicted flow $\hat{\boldsymbol{f}}_{i \to j} = \hat{\boldsymbol{p}}_j - \boldsymbol{p}_i$ from our optimized representation and the supervising input flow $\boldsymbol{f}_{i \to j}$ derived from running optical flow:

$$\mathcal{L}_{\text{flo}} = \sum_{\boldsymbol{f}_{i \to j} \in \Omega_f} ||\hat{\boldsymbol{f}}_{i \to j} - \boldsymbol{f}_{i \to j}||_1 \tag{3}$$

where Ω_f is the set of all the filtered pairwise flows. In addition, we minimize a photometric loss defined as the mean squared error (MSE) between the predicted color $\hat{\boldsymbol{C}}_i$ and the observed color $\boldsymbol{C}_i$ in the source video frame:

$$\mathcal{L}_{\text{pho}} = \sum_{(i, \boldsymbol{p}) \in \Omega_p} ||\hat{\boldsymbol{C}}_i(\boldsymbol{p}) - \boldsymbol{C}_i(\boldsymbol{p})||_2^2 \tag{4}$$

where Ω_p is the set of all pixel locations over all frames. Last, to ensure temporal smoothness of the 3D motion estimated by $M_{\boldsymbol{\theta}}$, we apply a regularization term that penalizes large accelerations. Given a sampled 3D location $\boldsymbol{x}_i$ in frame i, we map it to frame $i-1$ and frame $i+1$ using Eq. 1, yielding 3D points $\boldsymbol{x}_{i-1}$ and $\boldsymbol{x}_{i+1}$ respectively, and then minimize 3D acceleration as in [35]:

$$\mathcal{L}_{\text{reg}} = \sum_{(i, \boldsymbol{x}) \in \Omega_x} ||\boldsymbol{x}_{i+1} + \boldsymbol{x}_{i-1} - 2\boldsymbol{x}_i||_1 \tag{5}$$

where Ω_x is the union of local 3D spaces for all frames. Our final combined loss can be written as:

$$\mathcal{L} = \mathcal{L}_{\text{flo}} + \lambda_{\text{pho}}\mathcal{L}_{\text{pho}} + \lambda_{\text{reg}}\mathcal{L}_{\text{reg}} \tag{6}$$

where weights λ control the relative importance of each term.

The intuition behind this optimization is to leverage the bijections to a single canonical volume G, photo consistency, and the natural spatiotemporal smoothness provided by the coordinate-based networks $M_{\boldsymbol{\theta}}$ and $F_{\boldsymbol{\theta}}$ to reconcile inconsistent pairwise flow and fill in missing content in the correspondence graphs.

5.3. Balancing supervision via hard mining

The exhaustive pairwise flow input maximizes the useful motion information available to the optimization stage.

However, this approach, especially when coupled with the flow-filtering process, can result in an unbalanced collection of motion samples in dynamic regions. Rigid background regions typically have many reliable pairwise correspondences, while fast-moving and deforming foreground objects often have many fewer reliable correspondences after filtering, especially between distant frames. This imbalance can lead the network to focus entirely on dominant (simple) background motions, and ignore the challenging moving objects that represent a small portion of the supervisory signal.

To address this issue, we propose a simple strategy for mining hard examples during training. Specifically, we periodically cache flow predictions and compute error maps by calculating the Euclidean distance between the predicted and input flows. We use these error maps to guide our sampling process during optimization, such that regions with high errors are sampled more frequently. We compute these error maps on consecutive frames, where we assume our supervisory optical flow is most reliable. Please refer to the supplement for more details.

5.4. Implementation details

Network. Our mapping network $M_{\boldsymbol{\theta}}$ consists of six affine coupling layers. We apply positional encoding [41, 61] with 4 frequencies to the input coordinates in each layer before computing the scale and translation. We use a single 2-layer MLP with 256 channels implemented as a GaborNet [17] architecture to compute the latent code $\boldsymbol{\psi}_i$ for each frame i. The input to this MLP is the time t_i. The dimensionality of the latent code $\boldsymbol{\psi}_i$ is 128. The canonical representation $F_{\boldsymbol{\theta}}$ is also implemented using GaborNet [17], but with 3 layers of 512 channels.

Representation. We normalize all pixel coordinates $\boldsymbol{p}_i$ to the range $[-1, 1]$, and set the near and far depth range to 0 and 2, defining a local 3D space for each frame as $[-1, 1]^2 \times [0, 2]$. While our method can place content at arbitrary locations in the canonical space G, we initialize mapped canonical locations given by $M_{\boldsymbol{\theta}}$ to be roughly within a unit sphere to ensure well-conditioned input to the density/color network $F_{\boldsymbol{\theta}}$. To improve numerical stability during training, we apply the contraction operation in mip-NeRF 360 [3] to canonical 3D coordinates $\boldsymbol{u}$ before passing them to $F_{\boldsymbol{\theta}}$.

Training. We train our representation on each video sequence with the Adam optimizer [30] for 200k iterations. In each training batch, we sample 256 pairs of correspondences from 8 pairs of images resulting in 1024 correspondences in total. We sample $K = 32$ points on each ray using stratified sampling. More implementation details can be found in the supplementary material.

6. Evaluation

6.1. Benchmarks

We evaluate our method on the TAP-Vid benchmark [14], which is designed to evaluate the performance of point tracking across long video clips. TAP-Vid consists of both real-world videos with accurate human annotations of point tracks and synthetic videos with perfect ground-truth point tracks. Each point track is annotated through the entire video, and is labeled as occluded when not visible.

Datasets. We evaluate on the following datasets from TAP-Vid: 1) **DAVIS**, a real dataset of 30 videos from the DAVIS 2017 validation set [46], with clips ranging from 34-104 frames and an average of 21.7 point track annotations per video. 2) **Kinetics**, a real dataset of 1,189 videos each with 250 frames from the Kinetics-700-2020 validation set [10] with an average of 26.3 point track annotations per video. To make evaluation tractable for test-time optimization approaches like ours, we randomly sample a subset of 100 videos and evaluate all methods on this subset. 3) **RGB-Stacking** [31], a synthetic dataset of 50 videos each with 250 frames and 30 tracks. We exclude the synthetic Kubric dataset [20] as it is primarily intended for training. For quantitative evaluation, we adhere to the TAP benchmark protocol and evaluate all methods at 256×256 resolution, but all qualitative results are run at a higher resolution (480p).

Evaluation metrics. Following the TAP-Vid benchmark, we report both the position and occlusion accuracy of predicted tracks. We also introduce a new metric measuring temporal coherence. Our evaluation metrics include:

- $< \delta^x_{avg}$ measures the average position accuracy of visible points across 5 thresholds: 1, 2, 4, 8, and 16 pixels. The accuracy $< \delta^x$ at each threshold δ^x is the fraction of points that are within δ^x pixels of their ground truth position.

- **Average Jaccard (AJ)** evaluates both occlusion and position accuracy on the same thresholds as $< \delta^x_{avg}$. It categorizes predicted point locations as true positives, false positives, and false negatives, and is defined as the ratio of true positives to all points. True positives are points within the threshold of visible ground truth points. False positives are points that are predicted as visible, but where the ground truth is occluded or beyond the threshold. False negatives are ground truth visible points that are predicted as occluded or are beyond the threshold.

- **Occlusion Accuracy (OA)** evaluates the accuracy of the visibility/occlusion prediction at each frame.

- **Temporal Coherence (TC)** evaluates the temporal coherence of the tracks by measuring the L_2 distance between the acceleration of groundtruth tracks and predicted tracks. The acceleration is measured as the flow difference between two adjacent frames for visible points.

6.2. Baselines

We compare our method with various types of dense correspondence methods, including optical flow, feature matching, and multi-frame trajectory estimation as follows:

RAFT [62] is a state-of-the-art two-frame optical flow method. We consider two ways to use RAFT to generate multi-frame trajectories at test time: 1) chaining the RAFT predictions between consecutive frames into long-range tracks, which we call **RAFT-C**, and 2) directly computing RAFT flow between any (non-adjacent) query and target frames, which we call **RAFT-D**. When generating trajectories using RAFT-D, we always use the previous flow prediction as initialization for the current frame.

PIPs [21] is a method for estimating multi-frame point trajectories that can handle occlusions. By default, the method uses a temporal window of 8 frames, and longer trajectories must be generated through chaining. We used the official implementation of PIPs to perform chaining.

Flow-Walk [5] uses a multi-scale contrastive random walk to learn space-time correspondences by encouraging cycle consistency across time. Similar to RAFT, we report both chained and direct correspondence computation as **Flow-Walk-C** and **Flow-Walk-D**, respectively.

TAP-Net [14] uses a cost volume to predict the location of a query point in a single target frame, along with a scalar occlusion logit.

Deformable Sprites [74] is a layer-based video decomposition method. Like our method, it uses a per-video test-time optimization. However, it does not directly produce frame-to-frame correspondence, as the mapping from each frame to a canonical texture image is non-invertible. A nearest neighbor search in texture image space is required to find correspondence. Layered Neural Atlases [29] shares similarities to Deformable Sprites, but requires semantic segmentation masks as input, so we opt to compare to Deformable Sprites.

PIPs, TAP-Net and Deformable Sprites directly predict occlusion, but RAFT and Flow-Walk do not. Therefore we follow prior work [14, 73] and use a cycle consistency check with a threshold of 48 pixels to produce occlusion predictions for these methods. For our method, we detect occlusion by first mapping the query point to its corresponding 3D location in the target frame, then checking the transmittance of that 3D location in the target frame.

6.3. Comparisons

Quantitative comparisons. We compare our method to baselines on the TAP-Vid benchmark in Tab. 1. Our method achieves the best position accuracy, occlusion accuracy, and temporal coherence consistently across different datasets. Our method works well with different input pairwise corre-
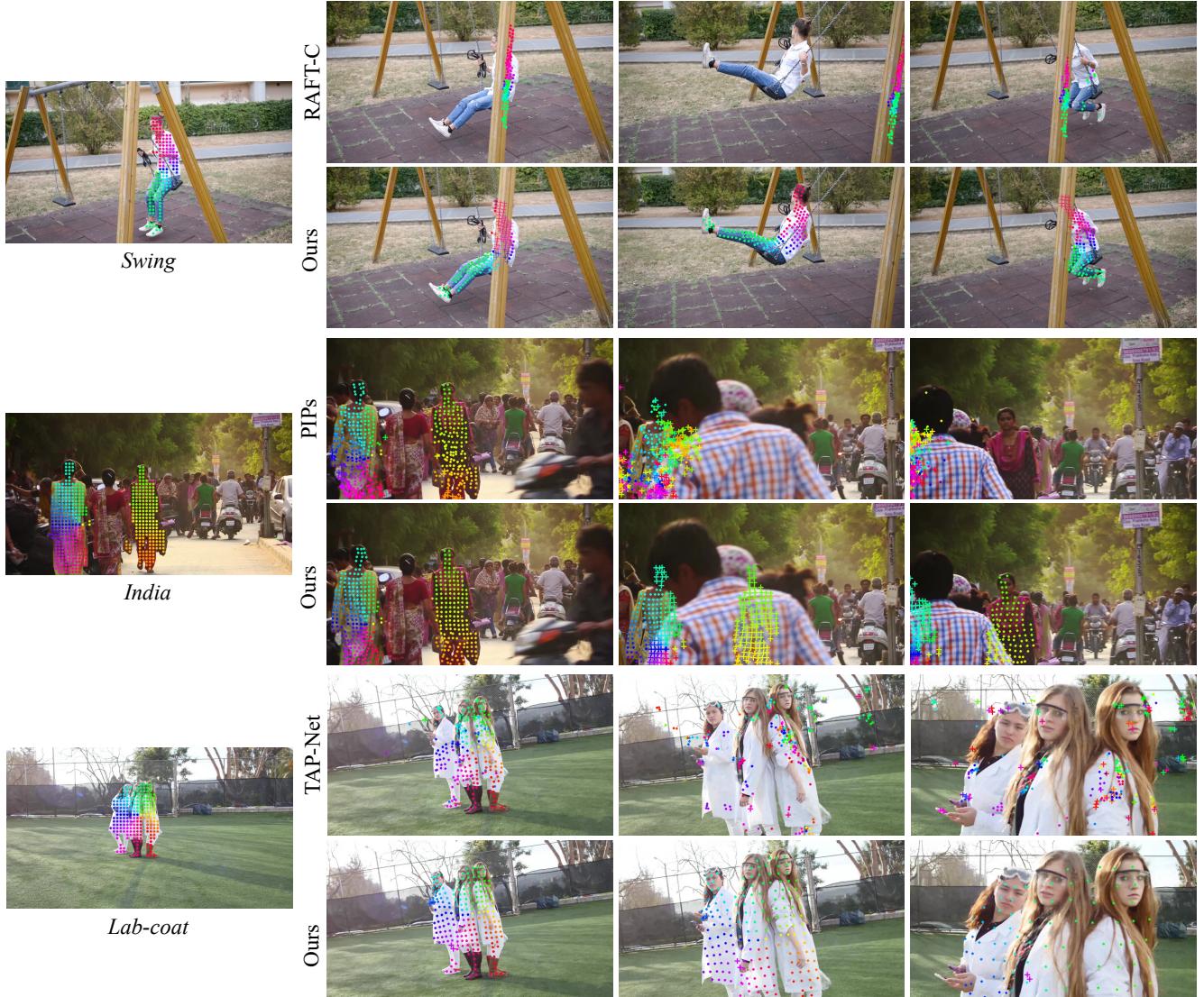
Figure 3: *Qualitative comparison of our method and baselines on DAVIS* [46]. The leftmost image shows query points in the first frame, and the right three images show tracking results over time. Notably, our method tracks successfully through the occlusion events in *swing* and *india*, while baseline methods fail. Our method additionally detects occlusion (marked as cross "+") and gives plausible location estimates even when a point is occluded. Please refer to the supplemental video for better visualizations of tracking accuracy and coherence.

spondences from RAFT and TAP-Net, and provides consistent improvements over both of these base methods.

Compared to approaches that directly operate on (non-adjacent) pairs of query and target frames, such as RAFT-D, TAP-Net, and Flow-Walk-D, our method achieves significantly better temporal coherence due to our globally consistent representation. Compared to chaining-based methods like RAFT-C, PIPs, and Flow-Walk-C, our method achieves better tracking performance, especially on longer videos. Chaining-based methods accumulate errors over time and are not robust to occlusion. Although PIPs considers a wider temporal window (8 frames) for better occlusion handling, it

fails to track a point if it remains occluded beyond the entire temporal window. In contrast, OmniMotion enables tracking points through extended occlusions. Our method also outperforms the test-time optimization approach Deformable Sprites [74]. Deformable Sprites decomposes a video using a predefined two or three layers with fixed ordering and models the background as a 2D atlas with a per-frame homography, limiting its ability to fit to videos with complex camera and scene motion.

Qualitative comparisons. We compare our method qualitatively to our baselines in Fig. 3. We highlight our ability to identify and track through (long) occlusion events while also

Table 1 (Kinetics, DAVIS, RGB-Stacking):

Method	Kinetics				DAVIS				RGB-Stacking			
	AJ ↑	$< \delta_{\mathrm{avg}}^{x}$ ↑	OA ↑	TC ↓	AJ ↑	$< \delta_{\mathrm{avg}}^{x}$ ↑	OA ↑	TC ↓	AJ ↑	$< \delta_{\mathrm{avg}}^{x}$ ↑	OA ↑	TC ↓
RAFT-C [62]	31.7	51.7	84.3	0.82	30.7	46.6	80.2	0.93	42.0	56.4	91.5	0.18
RAFT-D [62]	50.6	66.9	85.5	3.00	34.1	48.9	76.1	9.83	72.1	<u>85.1</u>	92.1	1.04
TAP-Net [14]	48.5	61.7	86.6	6.65	38.4	53.4	81.4	10.82	61.3	73.7	91.5	1.52
PIPs [21]	39.1	55.3	82.9	1.30	39.9	56.0	81.3	1.78	37.3	50.6	89.7	0.84
Flow-Walk-C [5]	40.9	55.5	84.5	<u>0.77</u>	35.2	51.4	80.6	0.90	41.3	55.7	<u>92.2</u>	<u>0.13</u>
Flow-Walk-D [5]	46.9	65.9	81.8	3.04	24.4	40.9	76.5	10.41	66.3	82.7	91.2	0.47
Deformable-Sprites [74]	25.6	39.5	71.4	1.70	20.6	32.9	69.7	2.07	45.0	58.3	84.0	0.99
Ours (TAP-Net)	<u>53.8</u>	<u>68.3</u>	<u>88.8</u>	<u>0.77</u>	<u>50.9</u>	<u>66.7</u>	**85.7**	0.86	<u>73.4</u>	84.1	<u>92.2</u>	**0.11**
Ours (RAFT)	**55.1**	**69.6**	**89.6**	**0.76**	**51.7**	**67.5**	<u>85.3</u>	**0.74**	**77.5**	**87.0**	**93.5**	<u>0.13</u>

Table 1: *Quantitative comparison of our method and baselines on the TAP-Vid benchmark* [14]. *We refer to our method as* Ours, *and present two variants,* Ours (TAP-Net) *and* Ours (RAFT), *which are optimized using input pairwise correspondences from TAP-Net* [14] *and RAFT* [62], *respectively. Both* Ours *and* Deformable Sprites [74] *estimate global motion via test-time optimization on each individual video, while all other methods estimate motion locally in a feed-forward manner. Our method notably improves the quality of the input correspondences, achieving the best position accuracy, occlusion accuracy, and temporal coherence among all methods tested.*

Method	AJ ↑	$< \delta_{\mathrm{avg}}^{x}$ ↑	OA ↑	TC ↓
No invertible	12.5	21.4	76.5	0.97
No photometric	42.3	58.3	84.1	0.83
Uniform sampling	47.8	61.8	83.6	0.88
Full	**51.7**	**67.5**	**85.3**	**0.74**

Table 2: Ablation study on DAVIS [46].

Figure 4: Pseudo-depth maps extracted from our representation, where blue indicates closer objects and red indicates further.

providing plausible locations for points during occlusion, as well as handling large camera motion parallax. Please refer to the supplementary video for animated comparisons.

6.4. Ablations and analysis

Ablations. We perform ablations to verify the effectiveness of our design decisions in Tab. 2. *No invertible* is a model variant that replaces our invertible mapping network $M_{\boldsymbol{\theta}}$ with separate forward and backward mapping networks between local and canonical frames (i.e., without the strict cycle consistency guarantees of our proposed bijections). While we additionally add a cycle consistency loss for this ablation, it still fails to construct a meaningful canonical space, and can only represent simple motions of the static background. *No photometric* is a version that omits the photometric loss $\mathcal{L}_{\mathrm{pho}}$; the reduced performance suggests the importance of photoconsistency for refining motion estimates. *Uniform sampling* replaces our hard-mining sampling strategy with a uniform sampling strategy, which we found leads to an inability to capture fast motion.

Analysis. In Fig. 4, we show pseudo-depth maps generated from our model to demonstrate the learned depth ordering. Note that these maps do not correspond to physical depth, nonetheless, they demonstrate that using only photometric and flow signals, our method is able to effectively sort out the relative ordering between different surfaces, which is
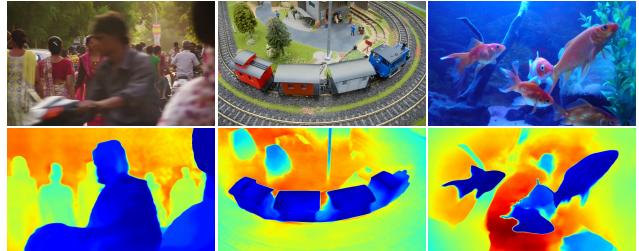
crucial for tracking through occlusions. More ablations and analyses are provided in the supplemental material.

7. Discussion and conclusion

Limitations. Like many motion estimation methods, our method struggles with rapid and highly non-rigid motion as well as thin structures. In these scenarios, pairwise correspondence methods can fail to provide enough reliable correspondences for our method to compute accurate global motion. In addition, due to the highly non-convex nature of the optimization problem, we observed that in some cases the training process can become trapped at sub-optimal solutions. Finally, our method in its current form can be computationally expensive. First, the flow collection process involves computing all pairwise flows exhaustively, which scales quadratically with respect to the sequence length. However, we believe the scalability of this process can be improved by exploring more efficient alternatives to exhaustive matching, e.g., vocabulary trees or keyframe-based matching, drawing inspiration from the Structure from Motion and SLAM literature. Second, like other methods that utilize neural implicit representations [41], our method involves a relatively long

optimization process. We believe that recent research in this area [42, 60] can help accelerate this process and allow further scaling to significantly longer sequences.

Conclusion. We proposed a new test-time optimization method for estimating complete and globally consistent motion for an entire video. We introduced a new video motion representation called OmniMotion which includes a quasi-3D canonical volume and per-frame local-canonical bijections. OmniMotion can handle general videos with varying camera setups and scene dynamics, and produce accurate and smooth long-range motion through occlusions. Our method achieves significant improvements over prior state-of-the-art methods both qualitatively and quantitatively.

References

[1] Sameer Agarwal, Yasutaka Furukawa, Noah Snavely, Ian Simon, Brian Curless, Steven M Seitz, and Richard Szeliski. Building rome in a day. *Communications of the ACM*, 54(10):105–112, 2011. 2

[2] Vijay Badrinarayanan, Fabio Galasso, and Roberto Cipolla. Label propagation in video sequences. In *Proc. Computer Vision and Pattern Recognition (CVPR)*, pages 3265–3272. IEEE, 2010. 2

[3] Jonathan T Barron, Ben Mildenhall, Dor Verbin, Pratul P Srinivasan, and Peter Hedman. mip-NeRF 360: Unbounded anti-aliased neural radiance fields. In *Proc. Computer Vision and Pattern Recognition (CVPR)*, pages 5470–5479, 2022. 5

[4] Herbert Bay, Andreas Ess, Tinne Tuytelaars, and Luc Van Gool. Speeded-up robust features (surf). *Computer vision and image understanding*, 110(3):346–359, 2008. 2

[5] Zhangxing Bian, Allan Jabri, Alexei A Efros, and Andrew Owens. Learning pixel trajectories with multiscale contrastive random walks. In *Proc. Computer Vision and Pattern Recognition (CVPR)*, pages 6508–6519, 2022. 2, 6, 8

[6] Michael J Black and Padmanabhan Anandan. A framework for the robust estimation of optical flow. In *Proc. Int. Conf. on Computer Vision (ICCV)*, pages 231–236. IEEE, 1993. 2

[7] Thomas Brox, Christoph Bregler, and Jitendra Malik. Large displacement optical flow. In *Proc. Computer Vision and Pattern Recognition (CVPR)*, pages 41–48, 2009. 2

[8] Thomas Brox and Jitendra Malik. Large displacement optical flow: descriptor matching in variational motion estimation. *Trans. Pattern Analysis and Machine Intelligence*, 33(3):500–513, 2010. 2

[9] Mathilde Caron, Hugo Touvron, Ishan Misra, Hervé Jégou, Julien Mairal, Piotr Bojanowski, and Armand Joulin. Emerging properties in self-supervised vision transformers. In *Proc. Int. Conf. on Computer Vision (ICCV)*, pages 9650–9660, 2021. 2, 12

[10] Joao Carreira and Andrew Zisserman. Quo vadis, action recognition? a new model and the kinetics dataset. In *Proc. Computer Vision and Pattern Recognition (CVPR)*, pages 6299–6308, 2017. 6

[11] Jason Chang, Donglai Wei, and John W Fisher. A video representation using temporal superpixels. In *Proc. Computer Vision and Pattern Recognition (CVPR)*, pages 2051–2058, 2013. 2

[12] Daniel DeTone, Tomasz Malisiewicz, and Andrew Rabinovich. Superpoint: Self-supervised interest point detection and description. In *Proc. Computer Vision and Pattern Recognition Workshops*, pages 224–236, 2018. 2

[13] Laurent Dinh, Jascha Sohl-Dickstein, and Samy Bengio. Density estimation using Real NVP. *arXiv preprint arXiv:1605.08803*, 2016. 4

[14] Carl Doersch, Ankush Gupta, Larisa Markeeva, Adria Recasens Continente, Kucas Smaira, Yusuf Aytar, Joao Carreira, Andrew Zisserman, and Yi Yang. Tap-vid: A benchmark for tracking any point in a video. In *NeurIPS Datasets Track*, 2022. 2, 4, 6, 8, 12

[15] Hugh Durrant-Whyte and Tim Bailey. Simultaneous localization and mapping: part i. *IEEE Robotics & Automation Magazine*, 13(2):99–110, 2006. 2

[16] Mihai Dusmanu, Ignacio Rocco, Tomas Pajdla, Marc Pollefeys, Josef Sivic, Akihiko Torii, and Torsten Sattler. D2-net: A trainable cnn for joint description and detection of local features. In *Proc. Computer Vision and Pattern Recognition (CVPR)*, pages 8092–8101, 2019. 2

[17] Rizal Fathony, Anit Kumar Sahu, Devin Willmott, and J Zico Kolter. Multiplicative filter networks. In *International Conference on Learning Representations*, 2021. 5

[18] Philipp Fischer, Alexey Dosovitskiy, Eddy Ilg, Philip Häusser, Caner Hazırbaş, Vladimir Golkov, Patrick Van der Smagt, Daniel Cremers, and Thomas Brox. Flownet: Learning optical flow with convolutional networks. *arXiv preprint arXiv:1504.06852*, 2015. 2

[19] Hang Gao, Ruilong Li, Shubham Tulsiani, Bryan Russell, and Angjoo Kanazawa. Monocular dynamic view synthesis: A reality check. In *Neural Information Processing Systems*, 2022. 3

[20] Klaus Greff, Francois Belletti, Lucas Beyer, Carl Doersch, Yilun Du, Daniel Duckworth, David J Fleet, Dan Gnanapragasam, Florian Golemo, Charles Herrmann, et al. Kubric: A scalable dataset generator. In *Proc. Computer Vision and Pattern Recognition (CVPR)*, pages 3749–3761, 2022. 6

[21] Adam W Harley, Zhaoyuan Fang, and Katerina Fragkiadaki. Particle video revisited: Tracking through occlusions using point trajectories. In *Proc. European Conf. on Computer Vision (ECCV)*, pages 59–75. Springer, 2022. 1, 2, 6, 8

[22] Berthold KP Horn and Brian G Schunck. Determining optical flow. *Artificial intelligence*, 17(1-3):185–203, 1981. 2

[23] Tak-Wai Hui, Xiaoou Tang, and Chen Change Loy. Liteflownet: A lightweight convolutional neural network for optical flow estimation. In *Proc. Computer Vision and Pattern Recognition (CVPR)*, pages 8981–8989, 2018. 2

[24] Eddy Ilg, Nikolaus Mayer, Tonmoy Saikia, Margret Keuper, Alexey Dosovitskiy, and Thomas Brox. Flownet 2.0: Evolution of optical flow estimation with deep networks. In *Proc.*

Computer Vision and Pattern Recognition (CVPR), pages 2462–2470, 2017. 2

[25] Michal Irani. Multi-frame optical flow estimation using subspace constraints. In *Proc. Int. Conf. on Computer Vision (ICCV)*, volume 1, pages 626–633, 1999. 2

[26] Allan Jabri, Andrew Owens, and Alexei Efros. Space-time correspondence as a contrastive random walk. In *Neural Information Processing Systems*, pages 19545–19560, 2020. 2

[27] Joel Janai, Fatma Guney, Anurag Ranjan, Michael Black, and Andreas Geiger. Unsupervised learning of multi-frame optical flow with occlusions. In *Proc. European Conf. on Computer Vision (ECCV)*, pages 690–706, 2018. 2

[28] Wei Jiang, Eduard Trulls, Jan Hosang, Andrea Tagliasacchi, and Kwang Moo Yi. Cotr: Correspondence transformer for matching across images. In *Proc. Int. Conf. on Computer Vision (ICCV)*, pages 6207–6217, 2021. 2

[29] Yoni Kasten, Dolev Ofri, Oliver Wang, and Tali Dekel. Layered neural atlases for consistent video editing. In *ACM Trans. Graphics (SIGGRAPH Asia)*, 2021. 2, 3, 6, 13

[30] Diederik P Kingma and Jimmy Ba. Adam: A method for stochastic optimization. *arXiv preprint arXiv:1412.6980*, 2014. 5

[31] Alex X Lee, Coline Manon Devin, Yuxiang Zhou, Thomas Lampe, Konstantinos Bousmalis, Jost Tobias Springenberg, Arunkumar Byravan, Abbas Abdolmaleki, Nimrod Gileadi, David Khosid, et al. Beyond pick-and-place: Tackling robotic stacking of diverse shapes. In *Proc. Conference on Robot Learning*, 2021. 6

[32] Jiahui Lei and Kostas Daniilidis. Cadex: Learning canonical deformation coordinate space for dynamic surface representation via neural homeomorphism. In *Proc. Computer Vision and Pattern Recognition (CVPR)*, pages 6624–6634, 2022. 4

[33] José Lezama, Karteek Alahari, Josef Sivic, and Ivan Laptev. Track to the future: Spatio-temporal video segmentation with long-range motion cues. In *Proc. Computer Vision and Pattern Recognition (CVPR)*, pages 3369–3376. IEEE, 2011. 2

[34] Xueting Li, Sifei Liu, Shalini De Mello, Xiaolong Wang, Jan Kautz, and Ming-Hsuan Yang. Joint-task self-supervised learning for temporal correspondence. In *Neural Information Processing Systems*, 2019. 2

[35] Zhengqi Li, Simon Niklaus, Noah Snavely, and Oliver Wang. Neural scene flow fields for space-time view synthesis of dynamic scenes. In *Proc. Computer Vision and Pattern Recognition (CVPR)*, pages 6498–6508, 2021. 2, 5

[36] Zhengqi Li and Noah Snavely. Megadepth: Learning single-view depth prediction from internet photos. In *Proc. Computer Vision and Pattern Recognition (CVPR)*, pages 2041–2050, 2018. 2

[37] Zhengqi Li, Qianqian Wang, Forrester Cole, Richard Tucker, and Noah Snavely. Dynibar: Neural dynamic image-based rendering. In *Proc. Computer Vision and Pattern Recognition (CVPR)*, 2022. 2

[38] Ce Liu, Jenny Yuen, and Antonio Torralba. Sift flow: Dense correspondence across scenes and its applications. *Trans. Pattern Analysis and Machine Intelligence*, 33(5):978–994, 2010. 2

[39] David G Lowe. Distinctive image features from scale-invariant keypoints. *Int. J. of Computer Vision*, 60:91–110, 2004. 2

[40] Bruce D Lucas and Takeo Kanade. An iterative image registration technique with an application to stereo vision. In *International Joint Conference on Artificial Intelligence*, volume 2, pages 674–679, 1981. 2

[41] Ben Mildenhall, Pratul P Srinivasan, Matthew Tancik, Jonathan T Barron, Ravi Ramamoorthi, and Ren Ng. NeRF: Representing scenes as neural radiance fields for view synthesis. *Communications of the ACM*, 65(1):99–106, 2021. 2, 3, 5, 8, 14

[42] Thomas Müller, Alex Evans, Christoph Schied, and Alexander Keller. Instant neural graphics primitives with a multiresolution hash encoding. In *ACM Trans. Graphics (SIGGRAPH)*, 2022. 9

[43] Keunhong Park, Utkarsh Sinha, Jonathan T Barron, Sofien Bouaziz, Dan B Goldman, Steven M Seitz, and Ricardo Martin-Brualla. Nerfies: Deformable neural radiance fields. In *Proc. Computer Vision and Pattern Recognition (CVPR)*, pages 5865–5874, 2021. 2

[44] Keunhong Park, Utkarsh Sinha, Peter Hedman, Jonathan T. Barron, Sofien Bouaziz, Dan B Goldman, Ricardo Martin-Brualla, and Steven M. Seitz. HyperNeRF: A higher-dimensional representation for topologically varying neural radiance fields. In *ACM Trans. Graphics (SIGGRAPH)*, 2021. 2

[45] Despoina Paschalidou, Angelos Katharopoulos, Andreas Geiger, and Sanja Fidler. Neural parts: Learning expressive 3d shape abstractions with invertible neural networks. In *Proc. Computer Vision and Pattern Recognition (CVPR)*, pages 3204–3215, 2021. 4

[46] Jordi Pont-Tuset, Federico Perazzi, Sergi Caelles, Pablo Arbeláez, Alex Sorkine-Hornung, and Luc Van Gool. The 2017 DAVIS challenge on video object segmentation. *arXiv preprint arXiv:1704.00675*, 2017. 6, 7, 8, 13

[47] René Ranftl, Katrin Lasinger, David Hafner, Konrad Schindler, and Vladlen Koltun. Towards robust monocular depth estimation: Mixing datasets for zero-shot cross-dataset transfer. *IEEE transactions on pattern analysis and machine intelligence*, 44(3):1623–1637, 2020. 13

[48] Zhile Ren, Orazio Gallo, Deqing Sun, Ming-Hsuan Yang, Erik B Sudderth, and Jan Kautz. A fusion approach for multi-frame optical flow estimation. In *Proc. Winter Conf. on Computer Vision (WACV)*, pages 2077–2086, 2019. 2

[49] Ignacio Rocco, Mircea Cimpoi, Relja Arandjelović, Akihiko Torii, Tomas Pajdla, and Josef Sivic. Neighbourhood consensus networks. In *Neural Information Processing Systems*, volume 31, 2018. 2

[50] Michael Rubinstein, Ce Liu, and William T Freeman. Towards longer long-range motion trajectories. In *Proc. British Machine Vision Conf. (BMVC)*, 2012. 2

[51] Peter Sand and Seth Teller. Particle video: Long-range motion estimation using point trajectories. *Int. J. of Computer Vision*, 80:72–91, 2008. 1, 2

[52] Johannes L Schonberger and Jan-Michael Frahm. Structure-from-motion revisited. In *Proc. Computer Vision and Pattern Recognition (CVPR)*, pages 4104–4113, 2016. 2

[53] Jianbo Shi et al. Good features to track. In *Proc. Computer Vision and Pattern Recognition (CVPR)*, pages 593–600. IEEE, 1994. 2

[54] Vincent Sitzmann, Julien Martel, Alexander Bergman, David Lindell, and Gordon Wetzstein. Implicit neural representations with periodic activation functions. In *Neural Information Processing Systems*, volume 33, pages 7462–7473, 2020. 2

[55] Noah Snavely, Steven M Seitz, and Richard Szeliski. Modeling the world from internet photo collections. *Int. J. of Computer Vision*, 80:189–210, 2008. 2

[56] Deqing Sun, Erik Sudderth, and Michael Black. Layered image motion with explicit occlusions, temporal consistency, and depth ordering. In *Neural Information Processing Systems*, volume 23, 2010. 2

[57] Deqing Sun, Xiaodong Yang, Ming-Yu Liu, and Jan Kautz. Pwc-net: Cnns for optical flow using pyramid, warping, and cost volume. In *Proc. Computer Vision and Pattern Recognition (CVPR)*, pages 8934–8943, 2018. 2

[58] Jiaming Sun, Zehong Shen, Yuang Wang, Hujun Bao, and Xiaowei Zhou. Loftr: Detector-free local feature matching with transformers. In *Proc. Computer Vision and Pattern Recognition (CVPR)*, pages 8922–8931, 2021. 2

[59] Narayanan Sundaram, Thomas Brox, and Kurt Keutzer. Dense point trajectories by GPU-accelerated large displacement optical flow. In *Proc. European Conf. on Computer Vision (ECCV)*, pages 438–451. Springer, 2010. 2

[60] Matthew Tancik, Vincent Casser, Xinchen Yan, Sabeek Pradhan, Ben Mildenhall, Pratul P Srinivasan, Jonathan T Barron, and Henrik Kretzschmar. Block-nerf: Scalable large scene neural view synthesis. In *Proc. Computer Vision and Pattern Recognition (CVPR)*, pages 8248–8258, 2022. 9

[61] Matthew Tancik, Pratul Srinivasan, Ben Mildenhall, Sara Fridovich-Keil, Nithin Raghavan, Utkarsh Singhal, Ravi Ramamoorthi, Jonathan Barron, and Ren Ng. Fourier features let networks learn high frequency functions in low dimensional domains. In *Neural Information Processing Systems*, volume 33, pages 7537–7547, 2020. 2, 5

[62] Zachary Teed and Jia Deng. Raft: Recurrent all-pairs field transforms for optical flow. In *Proc. European Conf. on Computer Vision (ECCV)*, pages 402–419, 2020. 2, 4, 6, 8, 12

[63] Carlo Tomasi and Takeo Kanade. Detection and tracking of point. *Int. J. of Computer Vision*, 9:137–154, 1991. 2

[64] Prune Truong, Martin Danelljan, and Radu Timofte. Glu-net: Global-local universal network for dense flow and correspondences. In *Proc. Computer Vision and Pattern Recognition (CVPR)*, pages 6258–6268, 2020. 2

[65] Prune Truong, Martin Danelljan, Luc Van Gool, and Radu Timofte. Learning accurate dense correspondences and when to trust them. In *Proc. Computer Vision and Pattern Recognition (CVPR)*, pages 5714–5724, 2021. 2

[66] Sebastian Volz, Andres Bruhn, Levi Valgaerts, and Henning Zimmer. Modeling temporal coherence for optical flow. In *Proc. Int. Conf. on Computer Vision (ICCV)*, pages 1116–1123. IEEE, 2011. 2

[67] Carl Vondrick, Abhinav Shrivastava, Alireza Fathi, Sergio Guadarrama, and Kevin Murphy. Tracking emerges by colorizing videos. In *Proc. European Conf. on Computer Vision (ECCV)*, pages 391–408, 2018. 2

[68] John YA Wang and Edward H Adelson. Layered representation for motion analysis. In *Proc. Computer Vision and Pattern Recognition (CVPR)*, pages 361–366, 1993. 2

[69] Qianqian Wang, Xiaowei Zhou, Bharath Hariharan, and Noah Snavely. Learning feature descriptors using camera pose supervision. In *Proc. European Conf. on Computer Vision (ECCV)*, pages 757–774, 2020. 2

[70] Xiaolong Wang, Allan Jabri, and Alexei A Efros. Learning correspondence from the cycle-consistency of time. In *Proc. Computer Vision and Pattern Recognition (CVPR)*, pages 2566–2576, 2019. 2

[71] Philippe Weinzaepfel, Jerome Revaud, Zaid Harchaoui, and Cordelia Schmid. DeepFlow: Large displacement optical flow with deep matching. In *Proc. Int. Conf. on Computer Vision (ICCV)*, pages 1385–1392, 2013. 2

[72] Wenqi Xian, Jia-Bin Huang, Johannes Kopf, and Changil Kim. Space-time neural irradiance fields for free-viewpoint video. In *Proc. Computer Vision and Pattern Recognition (CVPR)*, pages 9421–9431, 2021. 2

[73] Jiarui Xu and Xiaolong Wang. Rethinking self-supervised correspondence learning: A video frame-level similarity perspective. In *Proc. Int. Conf. on Computer Vision (ICCV)*, pages 10075–10085, 2021. 2, 6

[74] Vickie Ye, Zhengqi Li, Richard Tucker, Angjoo Kanazawa, and Noah Snavely. Deformable sprites for unsupervised video decomposition. In *Proc. Computer Vision and Pattern Recognition (CVPR)*, pages 2657–2666, 2022. 2, 3, 6, 7, 8

[75] Wang Zhao, Shaohui Liu, Hengkai Guo, Wenping Wang, and Yong-Jin Liu. ParticleSfM: Exploiting dense point trajectories for localizing moving cameras in the wild. In *Proc. European Conf. on Computer Vision (ECCV)*, pages 523–542, 2022. 2

[76] Tinghui Zhou, Philipp Krahenbuhl, Mathieu Aubry, Qixing Huang, and Alexei A Efros. Learning dense correspondence via 3d-guided cycle consistency. In *Proc. Computer Vision and Pattern Recognition (CVPR)*, pages 117–126, 2016. 2

A. Preparing pairwise correspondences

Our method uses pairwise correspondences from existing methods, such as RAFT [62] and TAP-Net [14], and consolidates them into dense, globally consistent, and accurate correspondences that span an entire video. As a preprocessing stage, we exhaustively compute all pairwise correspondences (i.e., between every pair of frames i and j) and filter them using cycle consistency and appearance consistency checks.

When computing the flow field between a base frame i and a target frame j as $i \rightarrow j$, we always use the flow prediction for the previous target frame ($i \rightarrow j - 1$) as initialization for the optical flow model (when possible). We find this improves flow predictions between distant frames. Still, the flow predictions between distant frames can contain significant errors, and therefore we filter out flow vector estimates with cycle consistency errors (i.e., forward-backward flow consistency error) greater than 3 pixels.

Despite this filtering process, we still frequently observe a persistent type of error that remains undetected by cycle consistency checks. This type of spurious correspondence, illustrated in Fig. 5, occurs because flow networks can struggle to estimate motion for regions that undergo significant deformation between the two input frames, and instead opt to interpolate motion from the surrounding areas. In the example in Fig. 5, this leads to flow on the foreground person "locking on" to the background layer instead. This behavior results in incorrect flows that survive the cycle consistency check, since they are consistent with a secondary layer's motion (e.g., background motion). To address this issue, we additionally use an appearance check: we extract dense features for each pixel using DINO [9] and filter out correspondences whose features' cosine similarity is < 0.5. In practice, we apply the cycle consistency check for all pairwise flows and supplement it with an appearance check when the two frames are more than 8 frames apart. We found this filtering process consistently eliminates major errors in flow fields across different sequences without per-sequence tuning. The results of our filtering approach, after both cycle and appearance consistency checks, are illustrated in Fig. 6.

One drawback of such a filtering process is that it will also remove correct flows for regions that become occluded in the target frame. For certain correspondence methods (such as RAFT), including these motion signals during occlusion events can result in better final motion estimates. Therefore, we devise a simple strategy for detecting reliable flow in occluded regions. For each pixel, we compute its forward flow to a target frame (a), cycle flow (flow back to the source frame from the target pixel) (b), and a second forward flow (c). This process effectively amounts to a 2-pass cycle consistency check: the consistency between (a) and (b) forms a standard cycle consistency check, and the consistency between (b) and (c) forms a secondary, supplementary

Figure 5: *Erroneous correspondences after cycle consistency check.* The red bounding box highlights a common type of incorrect correspondences from flow networks like RAFT [62] that remains undetected by cycle consistency check. The left images are query frames with query points and the right images are target frames with the corresponding predictions. Only correspondences on the foreground object are shown for better clarity.

Figure 6: *Correspondences from RAFT [62] after both cycle and appearance checks.* The left column shows a single query frame, and the right column displays target frames with increasing frame distances to the query frame from top to bottom. The filtered correspondences are reliable without significant errors.

one. We identify pixels where (a) and (b) are inconsistent but (b) and (c) are consistent and deem these to be occluded pixels. We found this approach effective in identifying reliable flows for occluded regions—particularly when the two frames are close to each other. Therefore, we allow these correspondences to bypass cycle consistency checks if they span a temporal distance of less than 3 frames. Our experiments use this added signal for the variant of our method that uses RAFT flow, but not for the TAP-Net variant, as we found the predicted correspondences from the latter were

Method	AJ $\uparrow$	$< \delta^x_{\mathrm{avg}} \uparrow$	OA $\uparrow$	TC $\downarrow$
Plain 2D	11.6	19.8	76.7	1.25
No invertible	12.5	21.4	76.5	0.97
No flow loss	23.9	37.3	70.8	1.75
No photometric	42.3	58.3	84.1	0.83
Uniform sampling	47.8	61.8	83.6	0.88
#Samples K = 8	48.1	63.5	84.6	0.75
#Samples K = 16	49.7	65.0	85.6	0.84
Full	**51.7**	**67.5**	**85.3**	**0.74**

Table 3: Ablation study on DAVIS [46].

less reliable near occlusion events.

We can also optionally augment the supervising input flow by chaining sequences of correspondences that are deemed reliable (i.e., those that satisfy the cycle consistency and appearance consistency checks). This helps densify the set of correspondences, creating supervision between distant frames where the direct flow estimates were deemed unreliable and therefore discarded during filtering. We found this process to be beneficial especially for challenging sequences with rapid motion or large displacements, where optical flow estimates between non-adjacent frames are less reliable.

B. Additional ablations

In addition to the ablations in the main paper, we provide the following ablations and report the results in Table 3: 1) *Plain 2D*: Rather than using a quasi-3D representation with bijections to model motion, we utilized a simple 8-layer MLP with 256 neurons that takes the query pixel location, query time, and target time as input and outputs the corresponding location in the target frame. Although we applied positional encoding with 8 frequencies to the input to enable better fitting, this ablation failed to capture the holistic motion of the video, instead only capturing simpler motion patterns for the rigid background. 2) *No flow loss*: we remove the flow loss and only rely on photometric information for training. We find this approach is effective only for sequences with small motion, where a photometric loss can provide useful signals to adjust motion locally. For sequences with relatively large motion, this method fails to provide correct results. 3) We also vary the number of samples K for each ray from 32 to 16 and 8. The resulting ablations, named *#Samples K=8* and *#Samples K=16*, demonstrate that using a denser sampling strategy tends to produce better results.

C. Additional implementation details

We provide additional implementation details below and will release our code upon acceptance.

Error map sampling. We cache the flow predictions generated by our model every 20k steps and use them to mine hard examples for effective training. Specifically, for each frame in the video sequence, we compute the optical flow between that frame and its subsequent frame, except for the final frame where we compute the flow between it and the previous frame. We then compute the L_2 distance between the predicted flow and supervising input flow, where each pixel in the video is now associated with a flow error. In each training batch, we randomly sampled half of the query pixels using weights proportional to the flow errors and the other half using uniform sampling weights.

Training details. In addition to the photometric loss $\mathcal{L}_{\mathrm{pho}}$ introduced in Sec. 5.2, we include an auxiliary loss term that penalizes discrepancies between the *differences* between the colors at pairs of pixels:

$$\mathcal{L}_{\mathrm{pgrad}} = \sum_{\Omega_p} ||(\hat{\boldsymbol{C}}_i(\boldsymbol{p}_1) - \hat{\boldsymbol{C}}_i(\boldsymbol{p}_2)) - (\boldsymbol{C}_i(\boldsymbol{p}_1) - \boldsymbol{C}_i(\boldsymbol{p}_2))||_1$$
(7)

This loss is akin to gradient losses that supplement pixel reconstruction losses in prior work [29, 47], but computed between pairs of randomly sampled, potentially distant pixels $\boldsymbol{p}_1$ and $\boldsymbol{p}_2$, rather than between adjacent pixels. We apply the same gradient loss to the flow prediction as well. We found that including these gradient losses can facilitate the training process.

We train our network with the Adam optimizer with base learning rates of 3×10^{-4}, 1×10^{-4}, and 1×10^{-3} for the density/color network $F_{\boldsymbol{\theta}}$, the mapping network $M_{\boldsymbol{\theta}}$, and the MLP that computes the latent code, respectively. We decrease the learning rate by a factor of 0.5 every 20k step. To select correspondences during training, we begin by sampling correspondences from pairs of frames with a maximum interval of 20, and gradually increase the window size during training. Specifically, we expand the window by one every 2k steps.

In our loss formulation, we compute the flow loss $\mathcal{L}_{\mathrm{flo}}$ as a weighted sum of the mean absolute error (MAE) between each pair of correspondences in a training batch. The weight is determined by the frame interval, and is given by $w = 1/\cos(\Delta/N' \cdot \pi/2)$, where Δ is the frame interval, and N' is the current window size. The coefficient λ_{pho} for the photometric loss initially starts at 0 and linearly increases to 10 over the first 50k steps of training. After 50k steps, λ_{pho} stays fixed at 10. This design is motivated by our observation that the photometric loss is not effective in fixing large motion errors early on in the training process, but is effective in refining the motion. The coefficient λ_{reg} for smoothness regularization is set to 20. We use the same set of network architecture and training hyperparameters when evaluating different datasets in the TAP-Net benchmark.

When sampling on each ray, we use a stratified sampling strategy and sample $K = 32$ points on each ray between the near and far depth range. Additionally, when mapping a 3D location from one local volume to another, we encourage
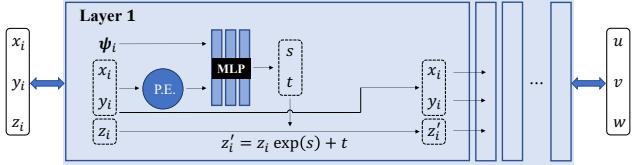
Figure 7: *Network architecture for the mapping network $M_{\boldsymbol{\theta}}$. We show the first affine coupling layer, which is representative of the subsequent layers, except for the different splitting patterns used. As mentioned in the main paper, this architecture is fully invertible, i.e., it can be queried in either direction, from (u, v, w) to (x, y, z) and vice-versa.*

it to be mapped within our predefined depth range to avoid degenerate solutions.

During training, we use alpha compositing to propagate the training signal to all samples along a ray. However, at inference time, we instead compute the corresponding location using the single sample with the largest alpha value, which we found to produce quantitatively similar but visually better results.

Network architecture for $M_{\boldsymbol{\theta}}$. We illustrate the architecture for our invertible network $M_{\boldsymbol{\theta}}$ that maps between local and canonical coordinate frames in Fig. 7. $M_{\boldsymbol{\theta}}$ is comprised of six affine coupling layers with alternating split patterns (only the first layer is highlighted in Fig. 7). The learnable component in each affine coupling layer is an MLP that computes a scale and a translation from a frame latent code ψ_i and the first part of the input coordinates. This scale and translation is then applied to the second part of the input coordinate. This process subsequently is repeated for each of the other coordinates. The MLP network in each affine coupling layer has 3 layers with 256 channels. We found that applying positional encoding [41] to the MLP's input coordinates improved its fitting ability, and we set the number of frequencies to 4.

Deformable sprites evaluation. Because the Deformable Sprites method defines directional mappings from image space to atlas space, we must approximate the inverses of these mappings in order to establish corresponding point estimates between pairs of frames. We do this by performing a nearest neighbor search: all points in the target frame are mapped to the atlas, and the closest atlas coordinate to the source point's mapping is chosen as the corresponding pixel. Furthermore, occlusion estimates are extracted using the following process: (1) initialize the layer assignment of source point tracks to the layer which has the higher opacity at the source frame, (2) at a given target frame index, denote the point as occluded if its originally assigned layer has lower opacity than the other layer.